Chinese Chemical Letters 35 (2024) 109644

Contents lists available at ScienceDirect

Chinese Chemical Letters

journal homepage: www.elsevier.com/locate/cclet

Urchin-like piezoelectric $ZnSnO_3/Cu_3P$ p-n heterojunction for enhanced cancer sonodynamic therapy

Qinyu Zhao[a,b,1], Yunchao Zhao[d,b,1], Songjing Zhong[b,c], Zhaoyang Yue[a,b], Zhuoheng Jiang[b,c], Shaobo Wang[a,b], Quanhong Hu[a,b], Shuncheng Yao[b,c], Kaikai Wen[b,c], Linlin Li[a,b,c,*]

[a] *School of Chemistry and Chemical Engineering, Guangxi University, Nanning 530004, China*
[b] *Beijing Institute of Nanoenergy and Nanosystems, Chinese Academy of Sciences, Beijing 101400, China*
[c] *School of Nanoscience and Engineering, University of Chinese Academy of Sciences, Beijing 100049, China*
[d] *College of Chemistry and Material Science, Shandong Agricultural University, Tai'an 271018, China*

ARTICLE INFO

Article history:
Received 12 December 2023
Revised 6 February 2024
Accepted 7 February 2024
Available online 10 February 2024

Keywords:
$ZnSnO_3$
Piezoelectric effect
Heterojunction
Chemodynamic therapy
Sonodynamic therapy
Reactive oxygen species

ABSTRACT

Sonodynamic therapy (SDT) exhibits noninvasive and accuracy in cancer treatment, and has aroused widespread attention. However, the low quantum yield of inorganic sonosensitizers under ultrasound (US) stimulation leads to unsatisfactory efficacy. In this work, an urchin-like piezoelectric $ZnSnO_3/Cu_3P$ p-n heterojunction was constructed as an efficient sonosensitizer for enhanced SDT. The p-n heterojunction formation narrows the band bandgap and increases the piezoelectric property, which contribute to the promotion of carrier separation and suppression of carrier recombination, resulting in enhanced SDT. Moreover, under tumor microenvironment (TME) with over produced H_2O_2 and glutathione (GSH), Cu_3P NNs induce chemodynamic therapy (CDT) by initiating a Fenton-like reaction and depleting GSH, leading to increased cellular oxidative damage. With the combination effect, the $ZnSnO_3/Cu_3P$ heterojunction demonstrates a 70% tumor growth inhibition rate in 4T1 tumor mice model. This piezoelectric heterojunction achieves the combined treatment of SDT and CDT, and opens new possibilities for the application of SDT in tumor therapy.

The fabrication of nanomaterials enables the production of cytotoxic reactive oxygen species (ROS), including singlet oxygen ($^1O_2$), superoxide anion ($^{\bullet}O_2^-$), and hydroxyl radicals ($^{\bullet}OH$), providing new methods to overcome the limitations of conventional tumor treatments [1–6]. One notable example is sonodynamic therapy (SDT), which utilizes sonosensitizers combined with ultrasound (US) stimulation to generate ROS, offering minimal invasiveness and high tumor specificity [7–11]. As a mechanical wave, US has advantages of precise orientation and long-distance propagation [12,13], thereby achieving deeper tissue penetration and higher spatial accuracy to reduce damage to normal tissues [14,15]. However, the development of SDT still encounter challenges related to low-efficiency ROS generation and the complicated tumor microenvironment (TME) [16,17]. Generally, overproduction of glutathione (GSH) in TME can consume the generated ROS, thereby discounting the efficacy of SDT [1,18,19]. Therefore, it is necessary to develop a more efficient sonosensitizers with TME responiveness to increase ROS generation and SDT therapeutic efficiency.

Recently, piezoelectric semiconductor nanomaterials, such as titanium oxide (TiO_2) [20], zinc oxide (ZnO) [21], barium titanate ($BaTiO_3$) [22,23], bismuth tungstate (Bi_2WO_6) [24,25], and bismuth oxychloride (BiOCl) [26], have gained recognition as a novel class of sonosensitizers for enhancing sonodynamic therapy (SDT). These piezoelectric materials can generate an inherently dynamic electric field under periodic mechanical forces, such as ultrasonic vibrations [27–29], which facilitates the separation of electrons (e^-) and holes (h^+), promoting the catalysis of ROS production [30]. Compared to nonpiezoelectric sonosensitizers, this inherently dynamic electric field piezoelectric semiconductor nanomaterials can efficiently reduce the recombination of carriers. And the band bending under US irradiation also promote the carrier separation and ROS production. Zinc stannate ($ZnSnO_3$) has attracted much attention in various piezoelectric materials because of its piezoelectric and ferroelectric properties, with an electrical and structural ordering temperature up to 700 °C [31–33]. $ZnSnO_3$ boasts an impressive polarization of approximately 59 $\mu C/cm^2$ along the c-axis, surpassing other non-lead-based piezoelectric

---

[*] Corresponding author.
E-mail address: lilinlin@binn.cas.cn (L. Li).
[1] These authors contributed equally to this work.

https://doi.org/10.1016/j.cclet.2024.109644

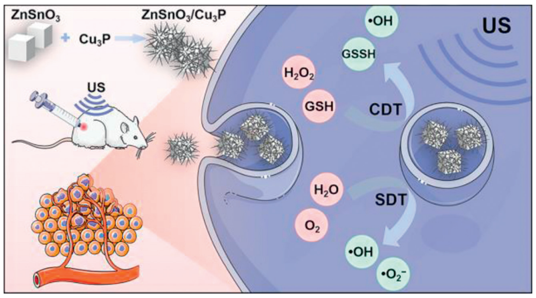

Scheme 1. Schematic depiction of the synthesis process and mechanism in the antitumor process of $ZnSnO_3/Cu_3P$ NCs.

materials such as and barium titanate ($BaTiO_3$, 6 μC/cm^2), zinc oxide (ZnO, 5 μC/cm^2), potassium niobate ($KNbO_3$, 23 μC/cm^2) [34,35]. Similar to other piezoelectric semiconductors, the challenge for $ZnSnO_3$ lies in the efficient separation of e^- and h^+ as well as preventing their recombination [36]. Development of $ZnSnO_3$ based piezoelectric sonosensitizers with high efficiency of e^- and h^+ seperation and ROS generation is highly desired.

In this work, an urchin-like piezoelectric p-n heterojunction was designed and synthesized by integrating p-type $ZnSnO_3$ nanocubes (NCs) and n-type Cu_3P nanoneedles (NNs) to form p-n heterojunction for enhancing cancer SDT (Scheme 1). The fabricated $ZnSnO_3/Cu_3P$ NCs effectively narrow the bandgap of $ZnSnO_3$ NCs, resulting in a higher redox activity to produce ROS. The urchin-like structure can further increase the US response to improve piezoelectric property. Additionally, Cu_3P NNs can respond to the TME, thereby consuming intracellular glutathione (GSH) and producing ROS through Fenton-like reaction to achieve CDT. Combining together, the piezoelectric p-n heterojunction realizes a 70% tumor growth inhibition rate on 4T1 tumor mice model by combining CDT and SDT. This piezoelectric p-n sonosensitizer opens the way for the construction and application of heterostructured nanomaterials in improving sonodynamic therapy. $ZnSnO_3$ NCs and Cu_3P NNs were prepared separately, and then $ZnSnO_3/Cu_3P$ heterojunction was formed by hydrothermal method (Fig. 1A) [37]. Scanning electron microscope (SEM) and transmission electron microscope (TEM) analysis revealed that $ZnSnO_3$ exhibited a uniform cubic shape, with average size of 71.9 ± 13.3 nm (Fig. 1B and Fig. S1 in Supporting information). Upon formation heterojunction with Cu_3P, the obtained $ZnSnO_3/Cu_3P$ NCs displayed an urchin-like morphology, with numerous nanoneedles radiating outward from the center (Fig. 1C). High-resolution transmission electron microscopy (HRTEM) image displayed the lattice widths of 0.25 nm corresponding to (102) crystal plane of Cu_3P and 0.33 nm corresponding to (012) crystal plane of $ZnSnO_3$ (Figs. 1D and E). Elemental mapping analysis confirmed that Cu and P elements were uniformly distributed on the surface of $ZnSnO_3$ (Fig. 1F and Fig. S2 in Supporting information). The phase structures of $ZnSnO_3$ and $ZnSnO_3/Cu_3P$ were characterized using X-ray diffraction (XRD), which revealed that only peaks corresponding to $ZnSnO_3$ (JCPDS No. 11-0274, Fig. S4 in Supporting information) was observed in the pattern of $ZnSnO_3/Cu_3P$, due to the low content of Cu_3P in the heterojunction (Fig. 1G). The chemical composition and valence state of the nanocubes were further analyzed by X-ray photoelectron spectroscopy (XPS). The XPS spectrum of $ZnSnO_3/Cu_3P$ displayed characteristic peaks of Zn 2p, Sn 3d, Cu 2p and P 2p at 1021.6, 486.2, 933.8 and 129.6 eV, respectively (Fig. 1H and Table S1 in Supporting information). In the high-resolution Cu 2p spectrum (Fig. 1I), the peaks at 932.8 and 934.8 eV corresponded to Cu(I) and Cu(II), respectively. The calculation results of peak area showed that the ratio of Cu(I) to Cu(II) content was approximately 85:15 (Table S2 in Supporting information). The valence states of Zn 2p, Sn 3d and O 1s in $ZnSnO_3/Cu_3P$ had no difference relative to $ZnSnO_3$ (Fig. 1J and Fig. S5 in Supporting information). Fourier transform infrared spectroscopy (FTIR) spectrum of $ZnSnO_3/Cu_3P$ showed that the characteristic peak of P—O bond appeared at 1100 cm^{-1}. This result indicates that Cu_3P have been successfully synthesized on the surface of $ZnSnO_3$ (Fig. S6 in Supporting information).

Table 1
First-order reaction kinetics of MB degradation under various treatments.

Group	US	$ZnSnO_3 + US$	$ZnSnO_3/Cu_3P + US$
Kinetic rate constant (k)	0.01131	0.03106	0.03620
Coefficient of determination (R^2)	0.93102	0.99260	0.99726

Dynamic light scattering (DLS) results illustrated that the mean hydrodynamic diameter of $ZnSnO_3$ was 215.7 nm, while that of $ZnSnO_3/Cu_3P$ slightly increased to 327.1 nm (Fig. 1K). Zeta potential of $ZnSnO_3$ changed from positive to negative upon the formation of $ZnSnO_3/Cu_3P$ heterojunction (Fig. 1L). Notably, the positive potential of $ZnSnO_3$ gradually decreased over time, while the zeta potential of $ZnSnO_3/Cu_3P$ remained stable, indicating better aqueous stability of the heterojunction. After dispersion of $ZnSnO_3/Cu_3P$ in phosphate buffer saline (PBS) solution at pH 6.5 for 24 h, a partial of nanoneedle on $ZnSnO_3/Cu_3P$ were fallen off from the nanocubes (Fig. S3 in Supporting information).

The ROS production of $ZnSnO_3/Cu_3P$ through sonodynamic, chemodynamic, and their combination processes was investigated (Fig. 2A). To evaluate the sonodynamic performance of $ZnSnO_3$ and $ZnSnO_3/Cu_3P$, methylene blue (MB) was chosen as an indicator that can be degraded by $^\bullet OH$ and superoxide anion ($^\bullet O_2^-$). After 10 min of US stimulation (1.0 MHz, 1.0 W/cm^2, 50% duty cycle), the presence of $ZnSnO_3$ or $ZnSnO_3/Cu_3P$ in the MB solutions resulted in significant degradation of MB (Fig. 2B and Fig. S6 in Supporting information), indicating that both $ZnSnO_3$ and $ZnSnO_3/Cu_3P$ NCs were capable of generating ROS under US stimulation. As shown in Fig. 2C, the first-order kinetic rate constant (k) of MB degradation by $ZnSnO_3/Cu_3P + US$ was 0.036 (Table 1), higher than that by US (0.011) and $ZnSnO_3 + US$ (0.031).

To identify the specific types of ROS produced during the SDT process, terephthalic acid (TA) and nitro tetrazolium blue chloride (NBT) were used as specific probes of $^\bullet OH$ and $^\bullet O_2^-$, respectively. After 10 min of US stimulation, the $^\bullet OH$ generation by $ZnSnO_3$ and $ZnSnO_3/Cu_3P$ NCs was approximately 1.82-fold and 2.34-fold higher than that in the mere US group (Fig. 2E and Fig. S8 in Supporting information), which correlated well with the results of MB degradation. Similarly, $ZnSnO_3/Cu_3P$ NCs produced a substantial amount of $^\bullet O_2^-$ under US stimulation (Fig. 2D and Fig. S7 in Supporting information). In contrast, the production of $^\bullet O_2^-$ $ZnSnO_3$ was substantially lower, similar with that by mere US stimulation. These results demonstrated that $ZnSnO_3/Cu_3P$ NCs can be excited by US irradiation to efficiently produce ROS, possessing superb SDT performance over $ZnSnO_3$. Also, the partial degradation of Cu_3P in a simulated tumor microenvironment (pH 6.5) did not affect the SDT performance of $ZnSnO_3/Cu_3P$ (Fig. S10 in Supporting information). The specific reactions involved in the sonodynamic process are shown below. Firstly, upon US irradiation, $ZnSnO_3/Cu_3P$ NCs, undergo polarization, leading to the segregation of electrons (e^-) and holes (h^+) (Eq. 1). Subsequently, nearby oxygen and water molecules react with these e^- and h^+, resulting in the formation of $^\bullet O_2^-$ and $^\bullet OH$ (Eqs. 2 and 3).

$$ZnSnO_3/Cu_3P \overset{US}{\rightarrow} ZnSnO_3/Cu_3P\left(e^- + h^+\right) \tag{1}$$

$$e^- + O_2 \rightarrow {}^\bullet O_2^- \tag{2}$$

$$h^+ + H_2O \rightarrow {}^\bullet OH + H^+ \tag{3}$$

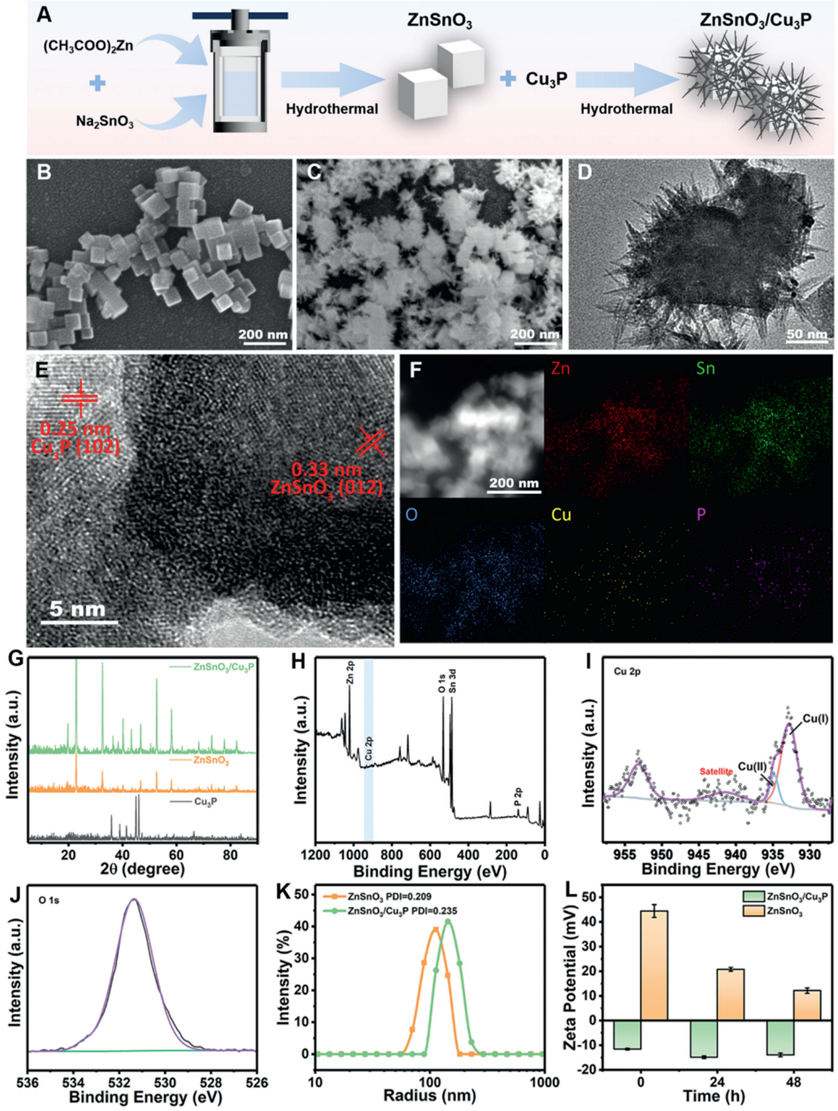

Fig. 1. Synthesis and characterizations of $ZnSnO_3/Cu_3P$. (A) Schematic diagram of the fabrication process of $ZnSnO_3/Cu_3P$. (B) SEM image of $ZnSnO_3$ NCs. (C) SEM image of $ZnSnO_3/Cu_3P$. (D) TEM image, (E) HRTEM image and (F) element mapping of $ZnSnO_3/Cu_3P$. (G) XRD, (H) XPS and high-resolution (I) Cu 2p and (J) O 1s XPS spectra of $ZnSnO_3/Cu_3P$. (K) hydrodynamic diameters and (L) zeta potential of $ZnSnO_3$ and $ZnSnO_3/Cu_3P$. The data represent means ± standard deviation (S.D.) ($n = 5$).

As previous reported, Cu(I) can initiate Fenton-like reaction and efficiently catalyze H_2O_2 to produce $^{\bullet}OH$, enabling chemodynamic therapy [38–43]. Given the presence of Cu(I) in $ZnSnO_3/Cu_3P$ NCs, we investigated the ROS generation in the presence of H_2O_2 under weakly acidic conditions. To assess this, 3,3′,5,5′-tetramethylbenzidine (TMB) was selected as a probe, which can react with $^{\bullet}OH$ to produce blue oxTMB. When mere H_2O_2 was added to the weakly acidic medium, the production of $^{\bullet}OH$ was negligible. Upon the addition of $ZnSnO_3/Cu_3P$ NCs, $^{\bullet}OH$ generation significantly increased. Furthermore, as the pH values decreased towards a more acidic conditions, $^{\bullet}OH$ production gradually increased (Fig. 2F). Hence, $ZnSnO_3/Cu_3P$ can serve as a potent chemodynamic agent for generating $^{\bullet}OH$, as depicted in Eq. 4.

$$Cu(I)+H_2O_2 \rightarrow Cu(II)+2^{\bullet}OH \qquad (4)$$

We further explored the synergistic effect of combining the sonodynamic and chemodynamic processes. We conducted a comparative analysis of MB degradation using $ZnSnO_3$ and $ZnSnO_3/Cu_3P$ NCs with both H_2O_2 and US irradiation. In MB solution containing H_2O_2 (pH 6.5), $ZnSnO_3/Cu_3P$ NCs induced simultaneous sonodynamic and chemodynamic processes under US irradiation. Remarkably, the integration of SDT and CDT exhibited a notable enhancement in ROS generation using $ZnSnO_3/Cu_3P$ NCs compared to the single sonodynamic or chemodynamic process (Fig. 2G and Fig. S8 in Supporting information). Consequently, the degradation of MB exhibited a faster first-order kinetic rate constant of 0.098, which was 2.7 times higher than of single SDT (Fig. 2H and Table 2). These finding demonstrated the enhanced efficiency of ROS generation through the combination effect, surpassing either SDT or CDT alone.

Additionally, electron spin resonance (ESR) spectroscopy was utilized to confirm the specific oxygen radicals produced in the combination process. For this purpose, a spin-trapping agent, 5,5-dimethyl-1-pyrroline *N*-oxide (DMPO), was utilized in either water or dimethyl sulfoxide to detect $^{\bullet}OH$ and $^{\bullet}O_2^-$, respectively. The DMPO/$^{\bullet}OH$ adduct exhibits a characteristic quadruple signal with a 1:2:2:1 amplitude ratio, while the DMPO/$^{\bullet}O_2^-$ adduct displays a characteristic multiple signals with a 1:1:1:1:1:1 amplitude ratio. In the presence of H_2O_2, $ZnSnO_3/Cu_3P$ displayed the highest signal intensity for both $^{\bullet}OH$ and $^{\bullet}O_2^-$ under US irradiation (Figs. 2I and J), verifying its superb combination effect of SDT and CDT.

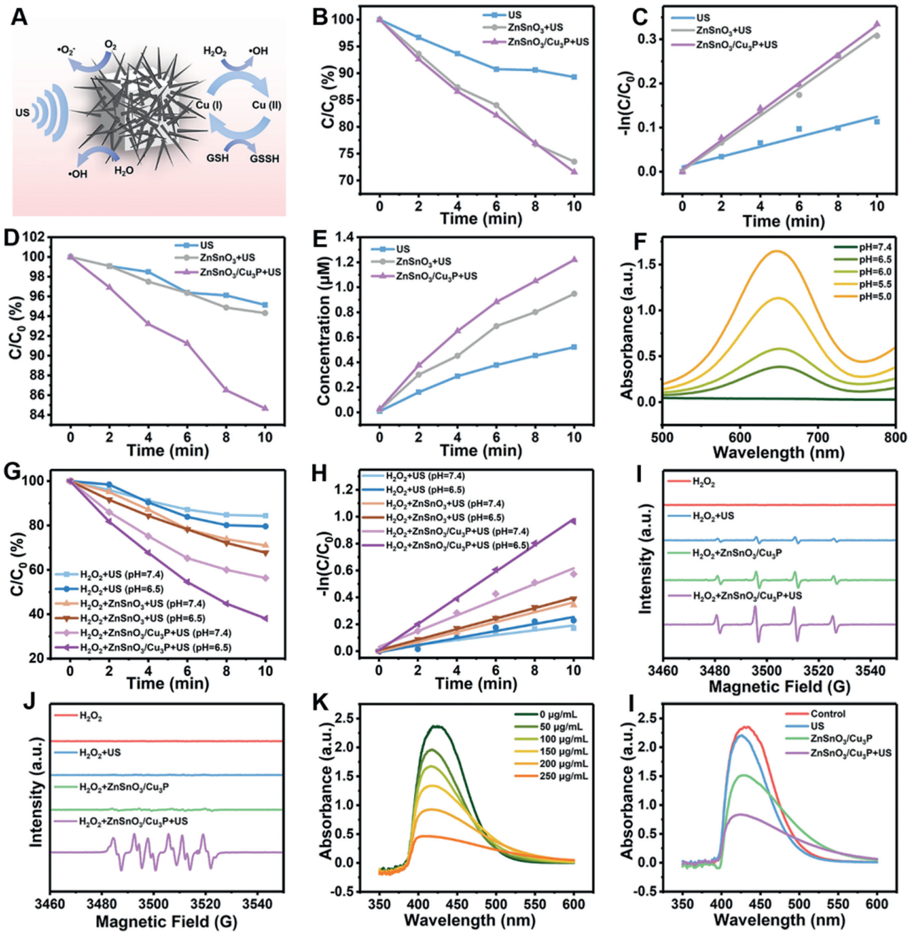

Fig. 2. Sonodynamic and chemodynamic performance of $ZnSnO_3/Cu_3P$. (A) Schematic representation illustrating the sonodynamic and chemodynamic processes of $ZnSnO_3/Cu_3P$. (B) Degradation curves of MB and (C) corresponding kinetic curves in SDT process. Degradation curves of NBT for $^{\bullet}O_2^-$ detection in the SDT process. (E) Generation of $^{\bullet}$OH in the SDT process with TA as the indicator. (F) Production of $^{\bullet}$OH in the CDT process measured with TMB as the indicator. (G) Degradation curves of MB and (H) corresponding kinetic curves in the combination process of SDT and CDT. ESR spectra of (I) $^{\bullet}$OH and (J) $^{\bullet}O_2^-$ trapped by DMPO under different conditions. (K) GSH oxidation by varying concentrations of $ZnSnO_3/Cu_3P$ within 3 h. (L) Oxidation of GSH achieved by combining SDT and CDT.

Table 2
First-order reaction kinetics of MB degradation under various treatments.

Group	H_2O_2 + US (pH 6.5)	H_2O_2 + US (pH 6.5)	H_2O_2 + $ZnSnO_3$ + US (pH 7.4)	H_2O_2 + $ZnSnO_3$ + US (pH 6.5)	H_2O_2 + $ZnSnO_3/Cu_3P$ + US (pH 7.4)	H_2O_2 + $ZnSnO_3/Cu_3P$ + US (pH 6.5)
k	0.01813	0.02619	0.03683	0.03911	0.05844	0.09780
R^2	0.95336	0.94698	0.98173	0.99789	0.97851	0.99869

In TME, GSH is overexpressed and acts as an antioxidant, which may hinder the therapeutic effect by ROS-induced oxidative damage [44]. Therefore, depletion of GSH in tumor tissue can enhance the oxidative stress and the efficacy of dynamic therapies. Considering the valence-variable nature of Cu, we assessed the capacity of $ZnSnO_3/Cu_3P$ to consume GSH. Upon incubating the GSH solution with $ZnSnO_3/Cu_3P$ NCs for 3 h, a significant decrease in GSH concentration was observed (Fig. 2K). Notably, GSH was depleted by 81% at a $ZnSnO_3/Cu_3P$ concentration of 250 μg/mL, indicating oxidative activity of Cu(II) in $ZnSnO_3/Cu_3P$ towards GSH. Furthermore, the addition of US stimulation further enhanced the degradation of GSH. When the concentration of $ZnSnO_3/Cu_3P$ was 250 μg/mL, 10 min of US stimulation (1.0 MHz, 1.0 W/cm^2, 50% duty cycle) before 1 h of resting leading to a 1.82-fold improvement in GSH consumption (Fig. 2L). The SDT and CDT properties of $ZnSnO_3/Cu_3P$ after 3 h of reaction with GSH were measured using MB and TMB as specific indicators. The reaction of $ZnSnO_3/Cu_3P$ with GSH had negligible impact on the SDT performance of $ZnSnO_3/Cu_3P$ (Fig. S12 in Supporting information), but improved its CDT performance (Fig. S13 in Supporting information). This may be due to the reduction of Cu(II) to Cu(I) in $ZnSnO_3/Cu_3P$ NCs, which improved the Fenton-like activity. Therefore, the synergistic effect of SDT and CDT was increased after treated with GSH (Fig. S14 in Supporting information). Taking together, $ZnSnO_3/Cu_3P$ NCs efficiently utilize the locally produced H_2O_2 in TME to catalyze the production of $^{\bullet}$OH through CDT. Second, the application of external US stimulation enhances the generation of both $^{\bullet}$OH and $^{\bullet}O_2^-$ through SDT. Third, the GSH consumption capacity of $ZnSnO_3/Cu_3P$ NCs can reduce the antioxidant activity of tumor cells. This combination holds great potential for augmenting cancer therapy.

In order to understand the mechanism of the SDT performance of $ZnSnO_3/Cu_3P$ NCs, the effect of piezotronic effect on carrier migration in $ZnSnO_3/Cu_3P$ NCs is analyzed in detail (Fig. 3A). First, the band structures of $ZnSnO_3$ and $ZnSnO_3/Cu_3P$ NCs were studied by ultraviolet−visible diffuse reflection spectra (UV−vis DRS). The

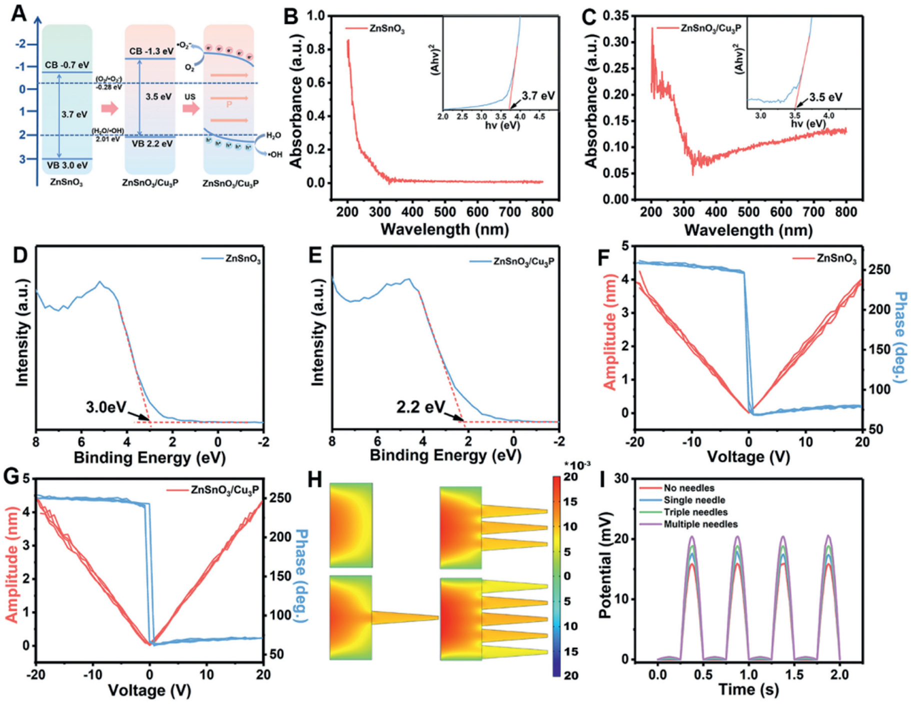

Fig. 3. Mechanism underlying the improved sonodynamic performance of $ZnSnO_3/Cu_3P$ NCs. (A) Schematic diagram illustrating the separation and migration of electron-hole pairs in both $ZnSnO_3$ NCs and $ZnSnO_3/Cu_3P$ NCs. UV–vis diffuse reflection spectra and results of Kubelka–Munk conversion of (B) $ZnSnO_3$ NCs and (C) $ZnSnO_3/Cu_3P$ NCs. XPS valence band spectra of (D) $ZnSnO_3$ NCs and (E) $ZnSnO_3/Cu_3P$ NCs. PFM phase hysteresis loop, and amplitude butterfly loop of (F) $ZnSnO_3$ NCs and (G) $ZnSnO_3/Cu_3P$ NCs. (H) COMSOL simulation of influence of surface nanoneedles (n = 0, 1, 3, and 5) on the electric potential under ultrasonic field and (I) statistics of the maximum surface potential.

bandgaps (E_g) of $ZnSnO_3$ and $ZnSnO_3/Cu_3P$ NCs were determined by analyzing the intercepts of the tangent and the abscissa in the Kubelka-Munk conversion. The calculated bandgaps were found to be 3.7 eV for $ZnSnO_3$ and 3.5 eV for $ZnSnO_3/Cu_3P$ (Figs. 3B and C). By examining the XPS valence band spectra, the valence band (VB) positions of $ZnSnO_3$ and $ZnSnO_3/Cu_3P$ were estimated to be 3.0 eV and 2.2 eV, respectively (Figs. 3D and E). Consequently, the conduction band (CB) positions of $ZnSnO_3$ and $ZnSnO_3/Cu_3P$ were determined as −0.7 eV and −1.3 eV, respectively.

The VB edge of pure $ZnSnO_3$ NCs (3.0 eV) was more positive than the $H_2O/{}^\bullet OH$ redox potential (2.01 eV *vs.* relative hydrogen electrode (RHE)), verifying that US-triggered h^+ on VB have the ability to react with H_2O to produce $^\bullet OH$. Similarly, the CB level (−0.7 eV) of $ZnSnO_3$ NCs is more negative compared with the redox potential of $O_2/{}^\bullet O_2{}^-$ (−0.28 V *vs.* RHE), indicating that the e^- generated by US can react with O_2 to produce $^\bullet O_2{}^-$. On the other hand, electron-hole pairs can rapidly recombine in pure $ZnSnO_3$ NCs, which leads to low efficiency of ROS production and SDT.

For $ZnSnO_3/Cu_3P$, the creation of p-n heterojunction effectively inhibited the recombination of e^- and h^+. More importantly, US can induce a built-in electric field that drives e^- and h^+ to opposite surfaces, leading to a band bending, which further promotes ROS generation. The piezoelectric properties of the $ZnSnO_3/Cu_3P$ heterojunction were assessed by piezoresponse force microscopy (PFM, Fig. S15 in Supporting information). The phase images acquired at an applied voltage of 20 V clearly demonstrate the presence of piezoelectricity of both $ZnSnO_3$ and $ZnSnO_3/Cu_3P$ (Figs. 3F and G). When a DC voltage ranging from −20 V to +20 V is applied, the PFM phase hysteresis loop exhibits a 180° phase change, indicating a ferroelectric polarization switching process. To further quantify the piezoelectric behavior, the piezoelectric coefficients (d_{33}) of $ZnSnO_3$ and $ZnSnO_3/Cu_3P$ NCs were measured using a typical amplitude butterfly loop method. The d_{33} values of $ZnSnO_3$ and $ZnSnO_3/Cu_3P$ NCs were about 200.0 and 219.5 pm/V, respectively. The results demonstrated that the piezoelectric response of $ZnSnO_3/Cu_3P$ was slightly enhanced compared with that of $ZnSnO_3$.

To investigate whether the needle-like structure on the surface of $ZnSnO_3/Cu_3P$ NCs enhanced the piezoelectric potential under an ultrasonic field, a COMSOL simulation was carried out (Figs. 3H and I). The simulation results showed that the more needle-like structures on the surface of $ZnSnO_3/Cu_3P$, the higher the US-induced piezoelectric potential, which may be due to the enhancement of mechanical effect on $ZnSnO_3$ NCs surface caused by needle-like structures. Therefore, we can summarize that $ZnSnO_3/Cu_3P$ p-n heterojunction can enhance the separation and migration of e^- and h^+ under US irradiation, improving the piezoelectric properties and thus enhancing the sonodynamic properties.

We validated the killing effect of $ZnSnO_3/Cu_3P$ NCs on tumor cells through the combination of SDT, CDT, and GSH consumption (Fig. 4A). First, L929 mouse fibroblasts were utilized to assess the cytotoxicity of $ZnSnO_3/Cu_3P$ NCs to normal cells. L929 cells remained an over 82% survival after 24 h incubation with $ZnSnO_3/Cu_3P$ NCs when the concentration reached 200 μg/mL (Fig. 4B). The cell viability of 4T1 mouse-derived breast cancer cells decreased to 30% after 24 h incubation with 200 μg/mL $ZnSnO_3/Cu_3P$ NC, which can be attributed to the CDT effect produced by higher H_2O_2 concentration in tumor cells. When US irradiation (1.0 MHz, 1.0 W/cm^2, 50% duty cycle) was imposed for 3 min, the cell killing rate remarkably increased to 80% (Fig. 4C). As shown in the biological TEM image (Fig. 4G), after endocytosis into the cells, $ZnSnO_3/Cu_3P$ NCs nanoparticles located in both bilayer phospholipid membrane vesicles and cytoplasm of the cells.

Calcein acetoxymethyl ester (calcein-AM) and propidium iodide (PI) were used for live/dead cell staining to further verify the cancer cell killing effect (Fig. 4D and Fig. S16 in Supporting information). The cell killing effect of mere US irradiation was negligible, while 31% of cells in the $ZnSnO_3/Cu_3P$ group died due to the CDT

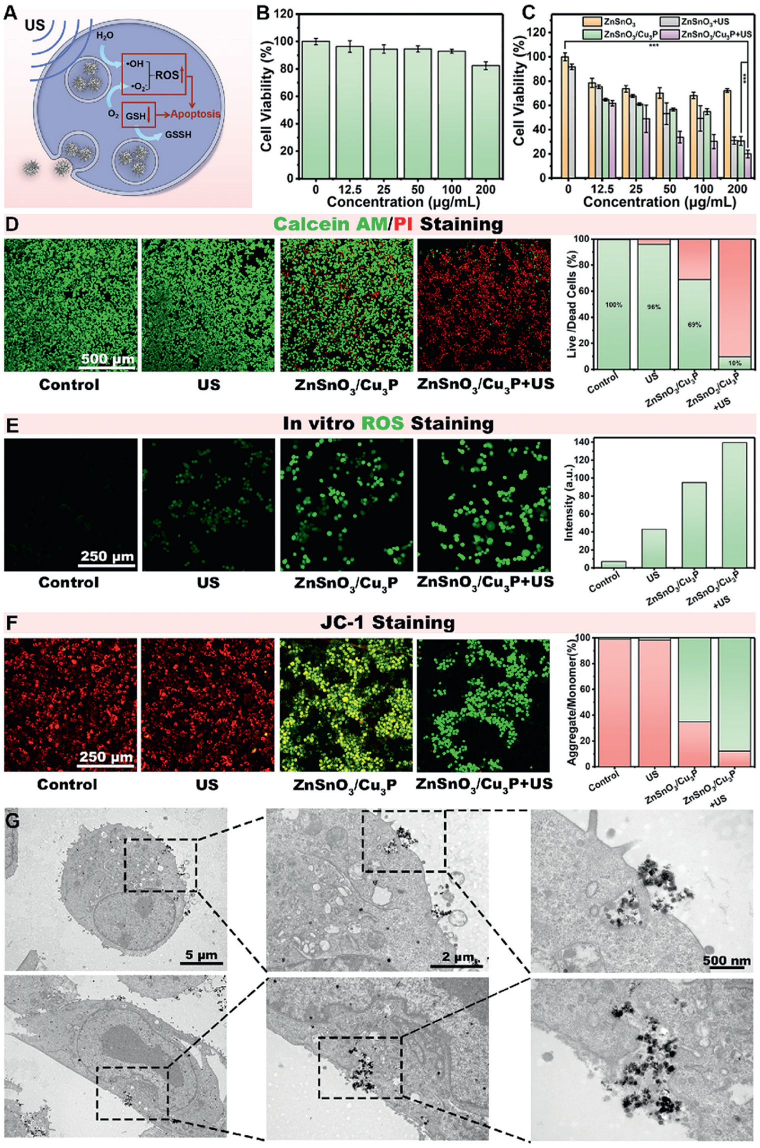

Fig. 4. *In vitro* cell experiments demonstrating the combined SDT and CDT performance of $ZnSnO_3/Cu_3P$ NCs for cancer cell killing. (A) Schematic representation depicting the mechanism of tumor cell killing by $ZnSnO_3/Cu_3P$ NCs through the integration of SDT and CDT. (B) Viabilities of L929 cells after treatments with $ZnSnO_3/Cu_3P$ NCs for 24 h. (C) Viability of 4T1 cells at 24 h post-treatment with different approaches. (D) Confocal images and green/red fluorescence (FL) ratios of Calcein AM/PI-stained 4T1 cells following various treatments. (E) Confocal images and corresponding quantitative analysis of intracellular ROS levels in 4T1 cells stained with DCFH-DA. (F) Confocal images and green/red FL ratios of JC-1-stained 4T1 cells. (G) Bio-TEM image of 4T1 cells after treatment with $ZnSnO_3/Cu_3P$ NCs for 10 h. The data represent means ± S.D. ($n = 5$). $^{***}P < 0.001$.

effect. In $ZnSnO_3/Cu_3P+US$ group, the percentage of dead cells was found to be 90%, which correlated with the results obtained from the MTT cell viability assay. 2′,7′-Dichlorodihydrofluorescein diacetate (DCFH-DA) was used as a fluorescence probe to evaluate the intracellular levels of reactive oxygen species (ROS) to gain further insights into the mechanism of cell killing. DCFH-DA can react with ROS to produce 2′,7′-dichlorofluorescein (DCF) which has green fluorescence. Compared to the US group, the intracellular fluorescence intensity in the $ZnSnO_3/Cu_3P$ and $ZnSnO_3/Cu_3P+US$ groups increased by 2.22-fold and 3.25-fold, respectively, demonstrating the capacity of $ZnSnO_3/Cu_3P$ NCs to generate abundant ROS *via* CDT and SDT especially under US activation (Fig. 4E).

Furthermore, to assess mitochondrial damage, the fluorescent probe 5,5′,6,6′-tetrachloro-1,1′,3,3′-tetraethyl-imidacarbocyanine iodide (JC-1) was employed to measure changes in mitochondrial membrane potential. Under normal conditions, JC-1 shows red fluorescence within intact mitochondrial membranes in the form of aggregates, while shows green fluorescence in damaged or depolarized mitochondria as monomers (Fig. S17 in Supporting information). As depicted in Fig. 4F, the $ZnSnO_3/Cu_3P$ group exhibited both green and red fluorescence in the mitochondria of 4T1 cells, whereas the $ZnSnO_3/Cu_3P+US$ group showed the strongest green fluorescence and red fluorescence, indicating significant mitochondrial oxidative damage.

Prior to investigating the *in vivo* antitumor activity of $ZnSnO_3/Cu_3P$ NCs, we evaluated their systemic toxicity. Acute toxicity experiments were performed by intravenously injecting female ICR mice with different doses of $ZnSnO_3/Cu_3P$ NCs (50, 100, 200 mg/kg). Throughout the 14-day observation period, all mice displayed similar clinical manifestations. The trend of weight change in the treatment groups was similar to that of the control group (Fig. S18 in Supporting information).

Blood biochemistry assay results showed that there were no abnormal changes in hepatic and renal function markers on the

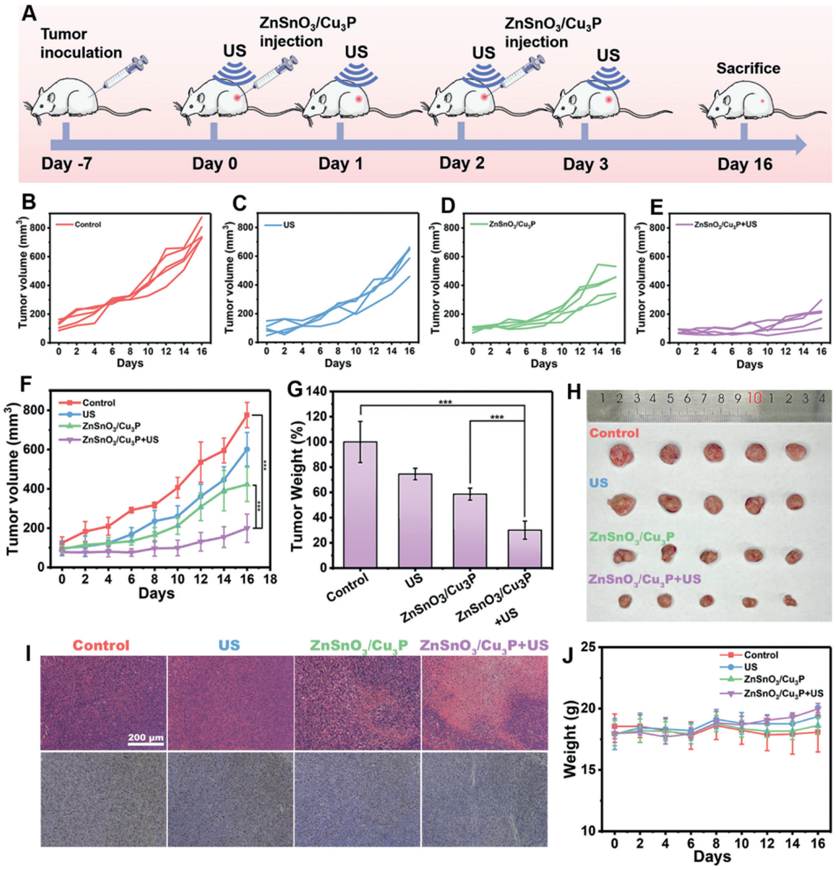

Fig. 5. *In vivo* cancer therapy on 4T1 tumor-bearing mice. (A) Schematic representation and timeline of the cancer treatment. (B–E) Individual tumor growth profiles and (F) average tumor growth profiles of mice following various treatments. (G) Average tumor weight and (H) representative tumor photographs from different groups on day 16. (I) H&E and Ki-67 staining of tumor sections in different groups. (J) Average body weight profiles. The data represent means ± S.D. ($n = 5$). ***$P < 0.001$.

14th day post-injection, including alanine aminotransferase (ALT), aspartate aminotransferase (AST), alkaline phosphatase (ALP), creatinine (CREA), and UREA, in mice injected with various doses of ZnSnO$_3$/Cu$_3$P NCs compared with those of mice in the control group. Blood routine test indicated normal levels of red blood cells (RBCs), hemoglobin (HGB), hematocrit (HCT), mean corpuscular volume (MCV), mean corpuscular hemoglobin (MCH), and platelets (PLT) in mice administered different doses of ZnSnO$_3$/Cu$_3$P NCs (Fig. S19 in Supporting information). Hematoxylin and eosin (H&E) staining revealed no histological abnormalities in major organs including heart, liver, spleen, lung and kidney in all mice, demonstrating the excellent biocompatibility of ZnSnO$_3$/Cu$_3$P NCs (Fig. S20 in Supporting information).

The *in vivo* anticancer efficacy of ZnSnO$_3$/Cu$_3$P NCs under US stimulation was assessed using a subcutaneous 4T1 tumor-bearing BALB/c mice model. All the procedures during the experiment firmly stuck to the "Beijing Administration Rule of Laboratory Animals" and the national standards "Laboratory Animal Requirements of Environment and Housing Facilities (GB 14925-2001)". The animal experiments were approved by the Committee on Ethics of Beijing Institute of Nanoenergy and Nanosystems (Approval Number: 2022A044). Mice which had been inoculated with tumor were randomly divided into four groups ($n = 5$): (1) PBS group; (2) PBS + US group, which intertumoral (i.t.) injection of PBS was followed by exposure to US irradiation; (3) ZnSnO$_3$/Cu$_3$P group, which received i.t. injection of 10 mg/kg ZnSnO$_3$/Cu$_3$P NCs; (4) ZnSnO$_3$/Cu$_3$P + US group, which i.t. injection of 10 mg/kg ZnSnO$_3$/Cu$_3$P NCs was followed by exposure to US irradiation. During the therapeutic period of 16 days, ZnSnO$_3$/Cu$_3$P NCs were administered twice on day 0 and day 2. Additionally, US irradiation (1.0 MHz, 2.5 W/cm^2, 3 min, 50% duty cycle) was applied four times during the initial 4 days (Fig. 5A).

Based on the tumor volume growth curves recorded over the 16-day treatment period (Figs. 5B–F), these were no significant differences in tumor growth rate between the PBS + US group and the PBS group. By comparison, moderate inhibition of tumor growth was observed in the ZnSnO$_3$/Cu$_3$P group, mainly attributed to CDT effect from ZnSnO$_3$/Cu$_3$P NCs. In contrast, the ZnSnO$_3$/Cu$_3$P + US group exhibited the highest level of tumor suppression. At the end of the treatment, the ZnSnO$_3$/Cu$_3$P + US group exhibited a tumor growth inhibition rate of 70% based on tumor weights (Figs. 5G and H), which was the highest of all the groups.

Histopathological H&E staining revealed extensive areas of tumor necrosis within the residual tissues of the tumors in the ZnSnO$_3$/Cu$_3$P + US group. Furthermore, Ki-67 immunohistochemical staining results showed a similar trend (Fig. 5I). Weight changes among all mice during the treatment exhibited no significant differences, indicating the compatibility and biosafety of the treatment modality (Fig. 5J). In addition, major organs such as the heart, liver, spleen, lung, and kidney exhibited no observable abnormalities or inflammation according to the results of H&E staining (Fig. S21 in Supporting information). These findings confirmed that ZnSnO$_3$/Cu$_3$P NCs, functioning as a sonosensitizer and chemodynamic agent, can achieve effective tumor therapy by combing SDT and CDT with a minimal systemic toxicity.

In summary, an urchin-like piezoelectric ZnSnO$_3$/Cu$_3$P p-n heterojunction has been successfully synthesized as a sonosensitizer for enhancing cancer SDT. The p-n heterojunction optimizes the energy band structure of ZnSnO$_3$/Cu$_3$P NCs and promotes the US sensitization performance. Additionally, Cu$_3$P exhibits chemodynamic activity and ability of GSH depletion, enabling the combination treatment of SDT and CDT. Ultimately, the piezoelectric sonosensitizer effectively generates ROS, reduces GSH, disrupts the redox balance within tumor cells, and promotes cell death, achieving satisfactory antitumor properties on 4T1 tumor-bearing BALB/c mice model. This strategy paves the way for constructing heterogeneous nanomaterials for cancer SDT therapy.

Declaration of competing interest

The authors declare that they have no known competing financial interests or personal relationships that could have appeared to influence the work reported in this paper.

Acknowledgments

The work was supported by the National Nature Science Foundation (No. 82072065), the Fundamental Research Funds for the Central Universities (No. E2EG6802X2), and the National Youth Talent Support Program.

Supplementary materials

Supplementary material associated with this article can be found, in the online version, at doi:10.1016/j.cclet.2024.109644.

References

[1] S. Bai, N.L. Yang, X.W. Wang, et al., ACS Nano 14 (2020) 15119–15130.
[2] Y.M. Ding, Z. Wang, Z.Y. Zhang, et al., Nano Res. 15 (2022) 7304–7312.
[3] Y. Zhao, T. Huang, X. Zhang, et al., BMEMat 1 (2023) e12006.
[4] D.D. Liu, X.L. Dai, W. Zhang, et al., Biomaterials 292 (2023) 121917.
[5] Y. Zhu, Y.J. Wang, G.R. Williams, et al., Adv. Sci. 7 (2020) 2000272.
[6] X. Xue, H. Qu, Y. Li, Exploration 2 (2022) 20210134.
[7] Y. Zhang, X.Q. Zhang, H.C. Yang, et al., Chem. Soc. Rev. 50 (2021) 11227–11248.
[8] L.A. Sun, X.W. Wang, F. Gong, et al., Theranostics 11 (2021) 9234.
[9] Y.Q. Yang, X.W. Wang, H.S. Qian, L. Cheng, Appl. Mater. Today 25 (2021) 101215.
[10] M.F. Wang, P.A. Ma, J. Lin, Chin. Chem. Lett. 34 (2023) 108300.
[11] T.T. Hu, W.C. Shen, F.Q. Meng, et al., Adv. Mater. 35 (2023) 2209692.
[12] A.B. Wu, L.D. Jiang, C. Xia, et al., Adv. Sci. 10 (2023) 2303016.
[13] A.Q. Ma, H.Q. Chen, Y.H. Cui, et al., Small 15 (2019) 1804028.
[14] S. Liang, X.R. Deng, P.A. Ma, Z.Y. Cheng, J. Lin, Adv. Mater. 32 (2020) 2003214.
[15] X.Q. Qian, Y.Y. Zheng, Y. Chen, Adv. Mater. 28 (2016) 8097–8129.
[16] Z.R. Gong, Z.F. Dai, Adv. Sci. 8 (2021) 2002178.
[17] X.H. Lin, J.B. Song, X.Y. Chen, H.H. Yang, Angew. Chem. Int. Ed. 59 (2020) 14212–14233.
[18] Y.F. Zhou, S.Y. Fan, L.L. Feng, X.L. Huang, X.Y. Chen, Adv. Mater. 33 (2021) 2104223.
[19] P.R. Zhao, H.Y. Li, W.B. Bu, Angew. Chem. Int. Ed. 62 (2023) e2022104.
[20] S.P. Ning, X.L. Dai, W.W. Tang, et al., Acta Biomater. 152 (2022) 562–574.
[21] Q.T. Hoang, V. Ravichandran, T.G.N. Cao, et al., Chem. Eng. J. 435 (2022) 135039.
[22] P. Zhu, Y. Chen, J.L. Shi, Adv. Mater. 32 (2020) 2001976.
[23] Y.C. Zhao, S.B. Wang, Y.M. Ding, et al., ACS Nano 16 (2022) 9304–9316.
[24] X.X. Deng, P. Chen, R.R. Cui, et al., Appl. Catal. B 339 (2023) 123148.
[25] H.Q. Ma, W.Y. Yang, S. Gao, et al., Chem. Eng. J. 455 (2023) 140471.
[26] J. Jang, K. Kim, J. Yoon, C.B. Park, Biomaterials 255 (2020) 120165.
[27] Z.L. Wang, Nano Today 5 (2010) 540–552.
[28] Z.L. Wang, Adv. Mater. 24 (2012) 4632–4646.
[29] Z.L. Wang, W.Z. Wu, Natl. Sci. Rev. 1 (2014) 62–90.
[30] S. Chen, P. Zhu, L.J. Mao, et al., Adv. Mater. 35 (2023) 2208256.
[31] Z.J. Wang, J. Liu, F.J. Wang, et al., J. Phys. Chem. C 114 (2010) 13577–13582.
[32] J. Zhang, K.L. Yao, Z.L. Liu, et al., Phys. Chem. Chem. Phys. 12 (2010) 9197–9204.
[33] Y. Inaguma, M. Yoshida, T. Katsumata, J. Am. Chem. Soc. 130 (2008) 6704.
[34] K.Y. Lee, D. Kim, J.H. Lee, et al., Adv. Funct. Mater. 24 (2014) 37–43.
[35] S. Shawon, Z.D. Carballo, V.S. Vega, et al., Nano Energy 92 (2022) 106653.
[36] X.S. Cao, M.X. Li, Q.Y. Liu, et al., Small 19 (2023) 2303195.
[37] G.R. Dillip, P.C. Nagajyothi, R. Ramaraghavulu, et al., Mater. Chem. Phys. 248 (2020) 122946.
[38] B.J. Ma, S. Wang, F. Liu, et al., J. Am. Chem. Soc. 141 (2019) 849–857.
[39] S.J. Zhong, C. Xiong, Y.C. Zhao, et al., Adv. Funct. Mater. 33 (2023) 2305625.
[40] Y.T. Zhao, L. Tao, Chin. Chem. Lett. 35 (2024) 108571.
[41] S. Wang, S.Q. Yang, Z.L. Cui, et al., Chem. Eng. J. 457 (2023) 141186.
[42] H. Lei, Z. Pei, C. Jiang, L. Cheng, Exploration 3 (2023) 20220001.
[43] D. Jana, Y. Zhao, Exploration 2 (2022) 20210238.
[44] J.A. Malla, R.M. Umesh, S. Yousf, et al., Angew. Chem. Int. Ed. 59 (2020) 7944–7952.